

1       **Focused Ultrasound Impels the Delivery and Penetration of Model**  
2                   **Therapeutics into Cerebral Cavernous Malformations**

3  
4  
5       **Delaney G. Fisher<sup>1,#</sup>, Matthew R. Hoch<sup>1,#</sup>, Catherine M. Gorick<sup>1</sup>, Claire Huchthausen<sup>2</sup>,**  
6                   **Victoria R. Breza<sup>1</sup>, Khadijeh A. Sharifi<sup>3,4</sup>, Petr Tvrdik<sup>3,4</sup>, G. Wilson Miller<sup>1,5</sup>,**  
7                                   **and Richard J. Price<sup>1,5</sup>**

8  
9  
10 # Authors contributed equally

11 1. Department of Biomedical Engineering, University of Virginia, Charlottesville, VA

12 2. Department of Physics, University of Virginia, Charlottesville, VA

13 3. Department of Neuroscience, University of Virginia, Charlottesville, VA

14 4. Department of Neurosurgery, University of Virginia Health System, Charlottesville, VA

15 5. Department of Radiology & Medical Imaging, University of Virginia, Charlottesville, VA

16

17

18

19

20 Corresponding Author:

21 Richard J. Price, Ph.D.

22 415 Lane Road, MR-5, Room 2316

23 Charlottesville, VA 22908.

24 Phone: 434-924-0020

25 Email: [rprice@virginia.edu](mailto:rprice@virginia.edu)

26

27 **Abstract**

28 **BACKGROUND:** Cerebral cavernous malformations (CCMs) are vascular neoplasms in the  
29 brain that can cause debilitating symptoms. Current treatments pose significant risks to some  
30 patients, motivating the development of new nonsurgical options. We recently discovered that  
31 focused ultrasound-mediated blood-brain barrier opening (FUS) arrests CCM formation and  
32 growth. Here, we build on this discovery and assess the ability of FUS to deliver model  
33 therapeutics into CCMs.

34 **METHODS:** Quantitative T1 mapping MRI sequences were used with 1 kDa (MultiHance; MH) and  
35 17 kDa (GadoSpin D; GDS) contrast agents to assess the FUS-mediated delivery and penetration  
36 of model small molecule drugs and biologics, respectively, into CCMs of Krit1 mutant mice.

37 **RESULTS:** FUS elevated the rate of MH delivery to both the lesion core (4.6-fold) and perilesional  
38 space (6.7-fold). Total MH delivery more than doubled in the lesion core and tripled in the  
39 perilesional space when FUS was applied immediately prior to MH injection. For the model  
40 biologic drug (i.e. GDS), FUS was of greater relative benefit, resulting in 21.7-fold and 3.8-fold  
41 delivery increases to the intralesional and perilesional spaces, respectively

42 **CONCLUSIONS:** FUS is capable of impelling the delivery and penetration of therapeutics into  
43 the complex and disorganized CCM microenvironment. Benefits to small molecule drug delivery  
44 are more evident in the perilesional space, while benefits to biologic delivery are more evident in  
45 CCM cores. These findings, when combined with ability of FUS alone to control CCMs, highlight  
46 the potential of FUS to serve as a powerful non-invasive therapeutic platform for CCM.

## 47 **Introduction**

48 Cerebral cavernous malformation (CCM) is a vascular disorder characterized by the  
49 development of abnormal, dilated clusters of blood vessels in the brain<sup>1</sup>. These malformations  
50 are prone to repetitive hemorrhages, inducing debilitating symptoms, such as neurological  
51 deficits, seizures, and stroke, in affected individuals<sup>2-4</sup>. Presently, the prevailing recourse for  
52 treating symptomatic CCMs is surgical resection. However, surgical excision of CCMs poses an  
53 elevated risk of complications and morbidity, evident by a distressing rate of surgical adverse  
54 events<sup>5,6</sup>.

55 Despite multiple studies investigating therapeutic targets and screening pharmacological  
56 treatments for CCM<sup>7,8,17,18,9-16</sup>, no approved drug treatments exist for CCM. The majority of tested  
57 pharmacological agents for CCM are small molecules. In comparison, larger biologic molecules,  
58 such as antibodies and gene therapies, have not been as well explored. Additionally, drugs  
59 showing promise in acute CCM models often demonstrate limited efficacy in more clinically-  
60 representative chronic models, suggesting a potential need for greater local doses of these  
61 therapies<sup>19,20</sup>. Indeed, though CCMs are known to be more permeable than healthy  
62 cerebrovasculature<sup>21-24</sup>, delivery of systemically administered drugs to these complex lesions is  
63 poorly understood.

64 Focused ultrasound-mediated blood-brain barrier opening (FUS) has emerged as a  
65 promising non-invasive drug delivery technology<sup>25-27</sup>. With FUS, acoustic energy is concentrated  
66 into a confined volume, facilitating the oscillation of intravenously administered gas-filled  
67 microbubbles within blood vessels of the targeted region. These microbubble oscillations induce  
68 a transient disruption of endothelial tight junctions<sup>28</sup> and increased active transport<sup>29</sup>, enabling  
69 therapeutic delivery across the blood-brain barrier (BBB). Magnetic resonance imaging (MRI)  
70 guidance permits spatial targeting of FUS to specific brain regions and BBB opening confirmation  
71 through the accumulation of gadolinium-based MRI contrast agents.

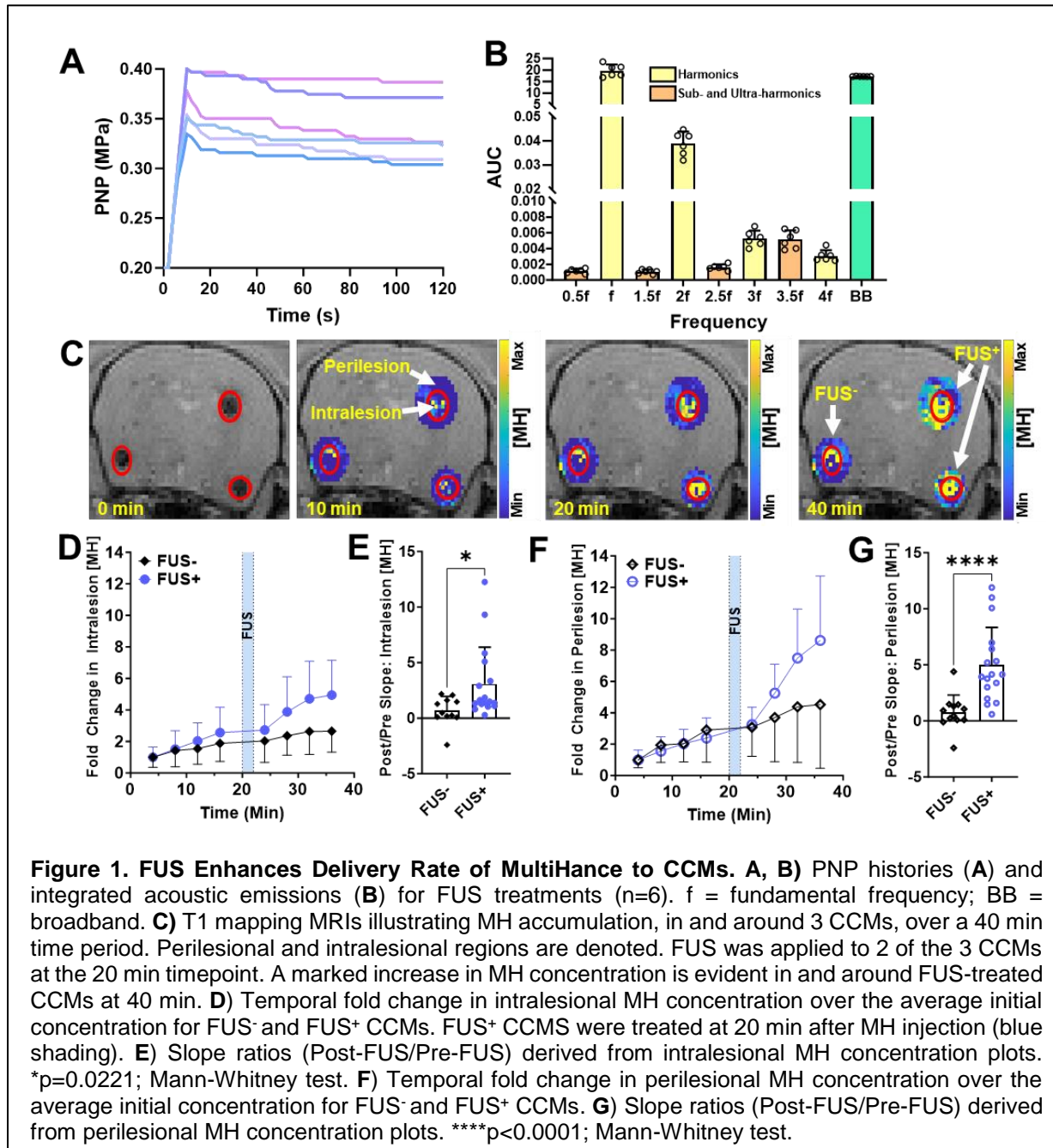
72           Recently, our group demonstrated that FUS, in the absence of therapeutic delivery, arrests  
73 the formation and growth of CCMs<sup>30</sup>. This remarkable observation prompts the exploration of the  
74 combined impact of FUS-mediated lesion stabilization and therapeutic delivery on CCMs. While  
75 our previous study also confirmed that FUS enhanced MRI contrast agent delivery beyond the  
76 natural permeability of CCMs, the MRI sequences only provided qualitative assessments. In  
77 particular, this qualitative MRI approach was sub-optimal for visualizing contrast agent delivery to  
78 the lesion core. Indeed, the cellular and molecular composition within the lesion core, including  
79 mutated endothelium, red blood cells, and their byproducts, differs substantially from the  
80 perilesional space, characterized by dense populations of astrocytes and microglia<sup>30,31</sup>. This  
81 difference not only affects MRI signal but may also have important implications for drug delivery  
82 to these distinct regions. Consequently, to facilitate comprehensive measurements of potential  
83 enhanced therapeutic delivery with FUS in the intricate CCM microenvironment, quantitative MRI  
84 methods are needed.

85           Building on our recent observations<sup>30</sup>, the objective of this study was to establish a  
86 foundation for therapeutic delivery approaches that harness and synergize with this potent  
87 bioeffect. We have previously demonstrated that T1-contrast mapping can enable longitudinal,  
88 quantitative concentration measurements of gadolinium-based molecules in CCMs<sup>31</sup>. Thus, this  
89 is an ideal method to measure FUS-induced changes for therapeutic delivery to CCMs. To this  
90 end, we employed T1-contrast mapping MRI to quantitatively evaluate the delivery of 1 kDa and  
91 17 kDa molecules to CCMs, comparing outcomes with and without FUS. This study lays the  
92 groundwork for treatment regimens capable of inducing CCM regression and clearance.

## 93 Results

### 94 FUS Enhances Delivery Rate of MultiHance in CCMs

95 We first tested if FUS would increase the delivery rate of a model small molecule drug to  
 96 the CCM microenvironment. To this end, we employed T1 mapping MRI to measure the  
 97 concentration of the MRI contrast agent MultiHance (MH; gadobenate dimeglumine; ~1 nm; ~1  
 98 kDa) before and after the application of FUS in CCM mice. One frontal hemisphere received FUS

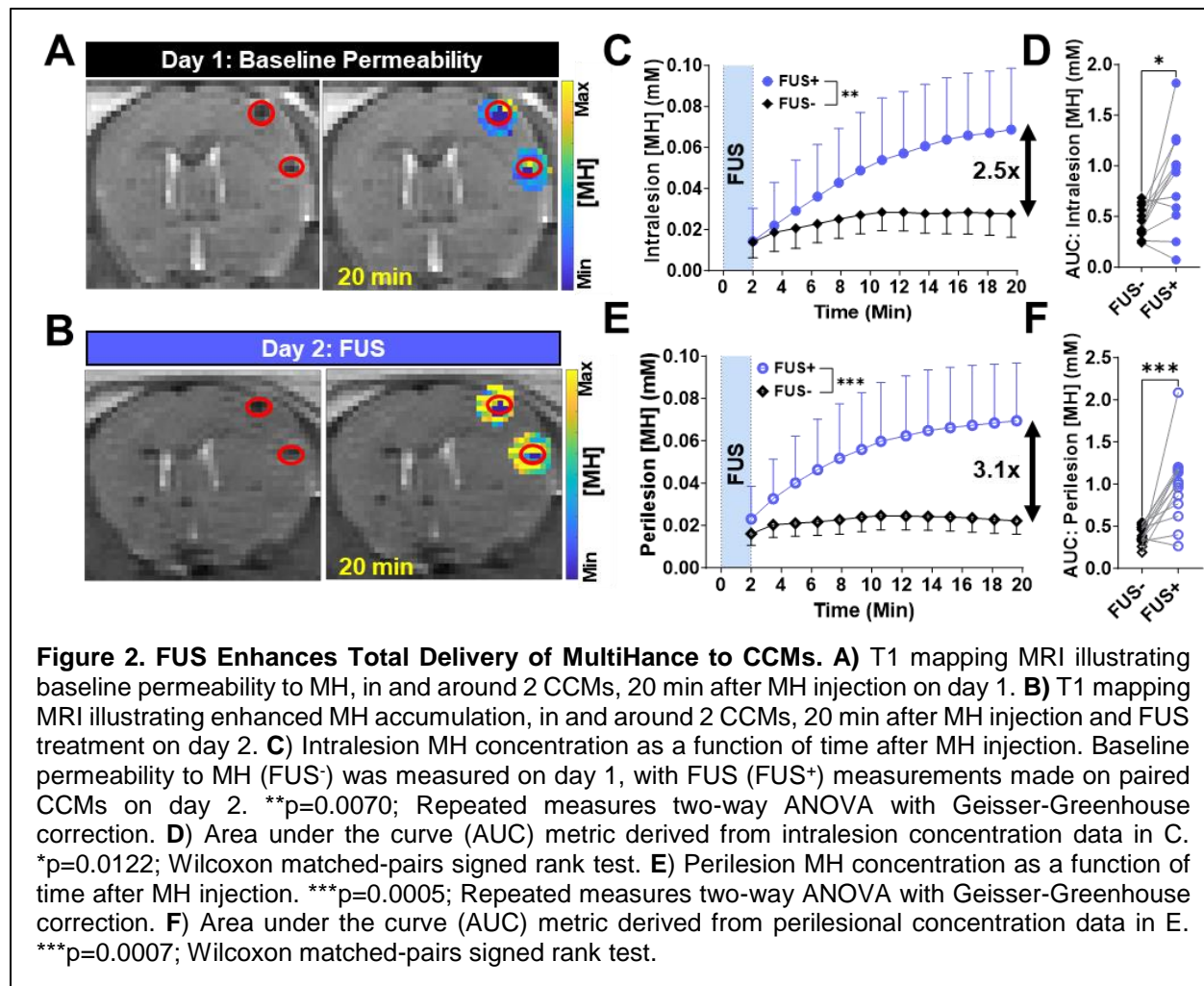


99 (n=6 sonication targets) with passive cavitation detection (PCD) feedback control 20 minutes after  
100 intravenous (i.v.) MH injection. During FUS, peak-negative pressures (PNPs) settled into a range  
101 of 0.3 to 0.4 MPa (**Figure 1A**), yielding integrated acoustic emissions shown in **Figure 1B**. The  
102 contralateral hemisphere was not sonicated (i.e., FUS<sup>-</sup> control) to illustrate baseline CCM  
103 permeability. As expected, prior to FUS, CCMs in the non-sonicated and sonicated hemispheres  
104 displayed similar rates of MH accumulation (**Figure 1C, D, F**). After FUS, the rate of MH  
105 accumulation in the lesion core was enhanced (**Figure 1D**), increasing to well-above (4.6-fold)  
106 the rate of MH accumulation in FUS<sup>-</sup> CCMs ( $p=0.0221$ ; **Figure 1E**). Predictably, the perilesional  
107 space of these CCMs also displayed the same permeability rate prior to FUS in both groups  
108 (**Figure 1F**). FUS then increased perilesional MH delivery rate by 6.7-fold over the rate of MH  
109 accumulation in FUS<sup>-</sup> CCMs ( $p<0.0001$ ; **Figure 1G**). These results indicate that FUS enhances  
110 the delivery rate of a model small molecule drug to both the lesion core and the surrounding CCM  
111 microenvironment.

112

### 113 **FUS Enhances Total Delivery of MultiHance in CCMs**

114 We then tested the ability of FUS to augment model small molecule drug delivery to CCMs  
115 using a protocol wherein the timing of i.v. MH injection with respect to FUS application was  
116 specifically chosen to yield more effective delivery. On day 1, T1 mapping MRI was conducted on  
117 CCM mice following i.v. MH injection to measure baseline permeability (**Figure 2A**). On day 2,  
118 FUS was applied to one frontal hemisphere of the same CCM mice immediately before i.v. MH  
119 injection. T1 mapping MRI was conducted for 20 mins thereafter (**Figure 2B**). FUS markedly  
120 boosted the intralesional MH delivery rate, as well as mean intralesional MH concentration  
121 ( $p=0.0070$ ; **Figure 2C**), with a 2.5-fold enhancement evident at 20 minutes. Area under the curve  
122 (AUC) analysis, representing the integrated exposure of CCM tissue to the model drug through  
123 time, indicates that FUS enhances intralesional model drug exposure by 1.9-fold ( $p=0.0122$ ;  
124 **Figure 2D**). Regarding the perilesional space, MH concentration was also markedly elevated with



125 FUS (p=0.0005; **Figure 2E**), with a 3.1-fold enhancement evident at 20 minutes. AUC yielded a  
 126 2.9-fold increase in model drug exposure over FUS<sup>-</sup> CCMs (p=0.0007; **Figure 2F**). Notably, MH  
 127 delivery after FUS becomes evident in the perilesional space (**Figure 2E**) before the intralésional  
 128 space (**Figure 2C**) (0.040 mM versus 0.029 mM, respectively, after 5 minutes), yet both locations  
 129 plateau to the same mean concentration by 20 mins post-injection (0.069 mM each). These  
 130 results reveal that FUS can more than double the amount of a small molecule delivered to the  
 131 lesion core and triple the amount in the surrounding CCM microenvironment.

132

133

134

### 135 FUS Enhances Total Delivery of GadoSpin D in CCMs

136 Next, we tested the potential for FUS to enhance the total delivery and penetration of a  
137 biologic, which are typically >1 kDa, to CCMs. To this end, we employed the MRI contrast agent  
138 GadoSpin D (GDS; dendritic Gd-chelate; ~5 nm; ~17 kDa) as a model biologic. As in the MH  
139 experiments (**Figure 2**), baseline permeability of CCMs to GDS was measured on day 1 (**Figure**  
140 **3A**). On day 2, FUS was applied to paired CCMs from day 1. FUS improved total GDS delivery in  
141 both the intralesional and perilesional spaces compared to baseline CCM permeability (**Figure**  
142 **3B**). FUS elicited a striking increase in GDS delivery to the lesion core ( $p=0.0106$ ; **Figure 3C**),  
143 reaching 21.7-fold at 20 minutes. AUC was increased 4.8-fold in CCM cores with FUS ( $p=0.0078$ ;  
144 **Figure 3D**). Meanwhile, perilesional delivery of GDS was also enhanced with FUS ( $p= 0.0021$ ;

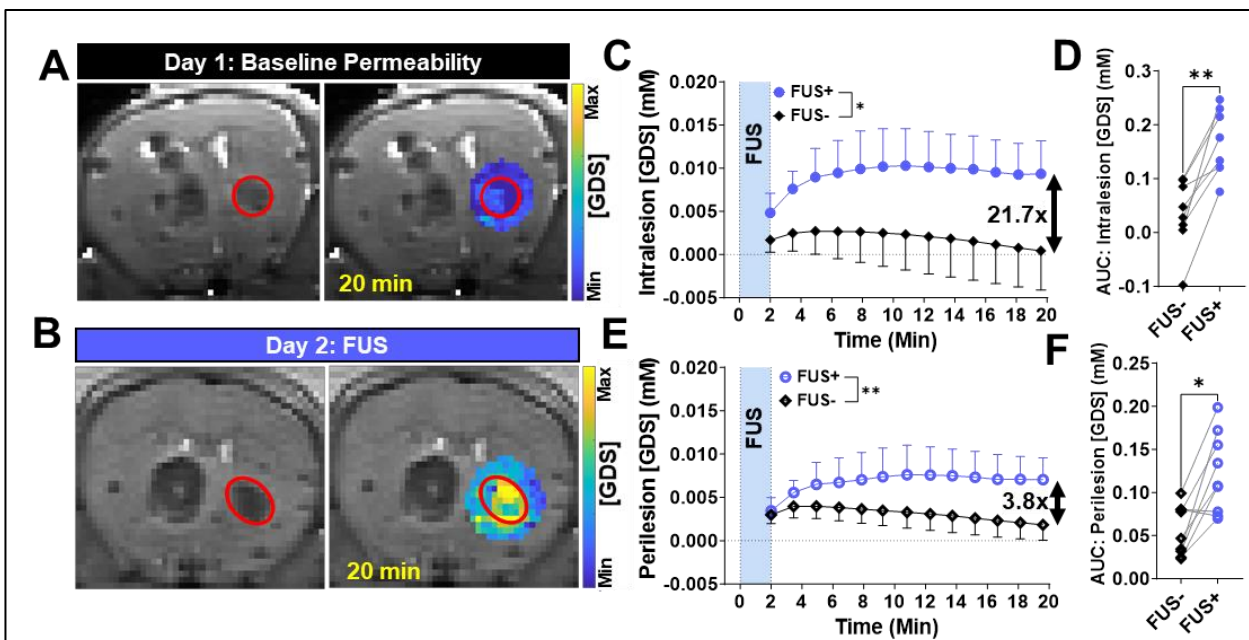


**Figure 3. FUS Enhances Total Delivery of Gadospin D in CCMs. A)** T1 mapping MRI illustrating baseline permeability to GDS, in and around a CCM, 20 min after GDS injection on day 1. **B)** T1 mapping MRI illustrating enhanced GDS accumulation, in and around a CCM, 20 min after GDS injection and FUS treatment on day 2. **C)** Intralesion GDS concentration as a function of time after GDS injection. Baseline permeability to GDS (FUS<sup>-</sup>) was measured on day 1, with FUS (FUS<sup>+</sup>) measurements made on paired CCMs on day 2. \* $p=0.0106$ ; Repeated measures two-way ANOVA with Geisser-Greenhouse correction. **D)** Area under the curve (AUC) metric derived from intralesion concentration data in C. \*\* $p=0.0078$ ; Wilcoxon matched-pairs signed rank test. **E)** Perilesion GDS concentration as a function of time after GD injection. \*\* $p=0.0021$ ; Repeated measures two-way ANOVA with Geisser-Greenhouse correction. **F)** Area under the curve (AUC) metric derived from perilesional concentration data in E. \* $p=0.0195$ ; Wilcoxon matched-pairs signed rank test.

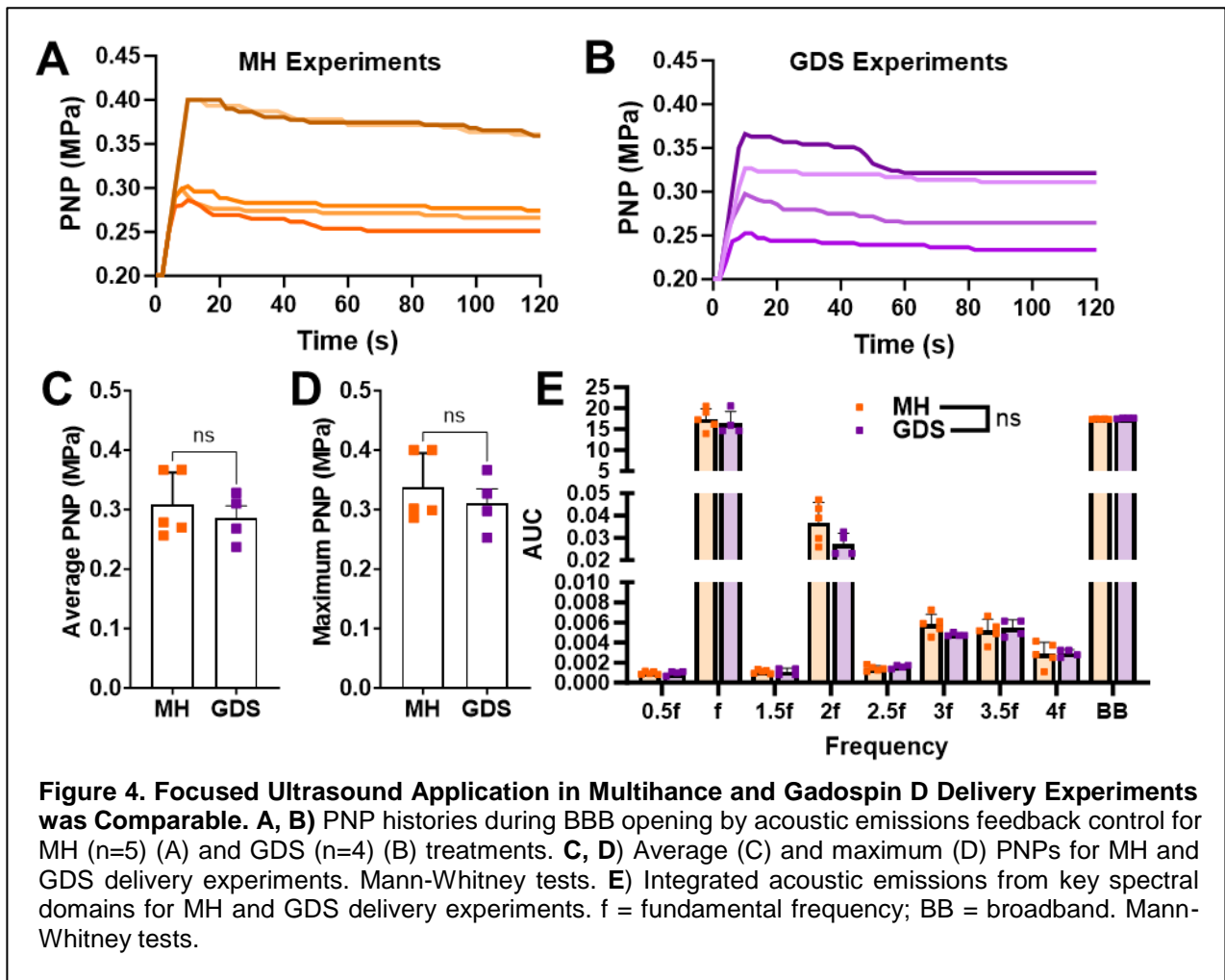


145 **Figure 3E**), reaching a 3.8-fold increase at 20 minutes. For GDS in the perilesional space,  
146 integrated tissue-drug exposure increased 2.2-fold ( $p=0.0195$ ; **Figure 3F**). The lesion core and  
147 perilesional space followed a similar temporal pattern of GDS enhancement following FUS, but  
148 the intralesional space peaked at a higher concentration than the perilesional space (0.010 mM  
149 versus 0.0076 mM, respectively).

150

### 151 **Comparison of FUS-Mediated MultiHance and GadoSpin D Delivery to Intralesion and** 152 **Perilesion CCM Compartments**

153 We also investigated whether FUS differentially affects the delivery of MH and GDS to  
154 intralesion and perilesion regions of CCMs. To this end, we first needed to verify that the applied



155 FUS PNP, as well as the resultant MB activity, were equivalent in the MH and GDS experiments.  
156 The PNP histories for the MH (Figure 4A) and GDS (Figure 4B) experiments followed similar  
157 trajectories, and there were no differences in average (Figure 4C) and maximum (Figure 4D)

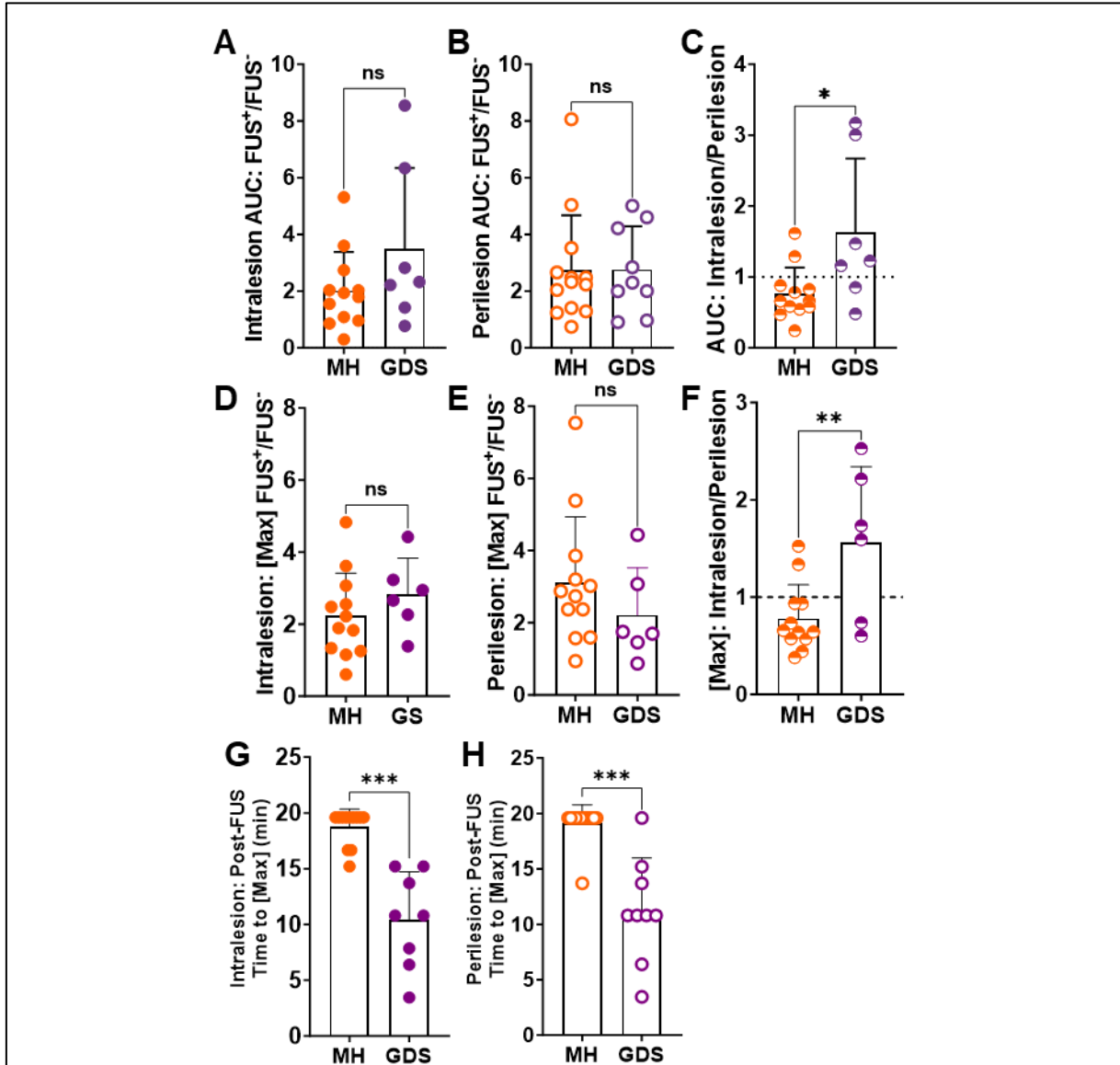


**Figure 5. Comparison of FUS-Mediated MultiHance and GadoSpin D Delivery to Intralesion and Perilesion CCM Compartments.** A, B) Intralesion (A) and perilesion (B) AUC ratios (FUS<sup>+</sup>/FUS<sup>-</sup>) for MH and GDS. Mann-Whitney tests. C) Intralesion/perilesion ratios of AUC ratios for MH and GDS. \*p=0.045; Mann-Whitney test. D, E) Intralesion (D) and perilesion (E) maximum concentration ratios (FUS<sup>+</sup>/FUS<sup>-</sup>) for MH and GDS. Mann-Whitney tests. F) Intralesion/perilesion ratios of maximum concentration ratios for MH and GDS. \*p=0.025; Mann-Whitney test. G, H) Intralesion (G) and perilesion (H) post-FUS time to maximum concentration for MH and GDS. \*\*\*p<0.001; Mann-Whitney tests.

158 applied PNP. Moreover, MB activity, as assessed by acoustic emissions across several key  
159 spectral domains (i.e. sub-harmonic, harmonic, ultra-harmonic, and broadband), was equivalent  
160 for the MH and GDS experiments. Thus, any differences between MH and GDS delivery were not  
161 due to differences in FUS application and/or MB response.

162 When comparing GDS to MH delivery using the AUC metric, similar levels of FUS-  
163 mediated delivery enhancement (i.e. FUS<sup>+</sup>/FUS<sup>-</sup>) to both the intralesional (**Figure 5A**) and  
164 perilesional spaces (**Figure 5B**) were observed, with GDS exhibiting a slight trend ( $p=0.23$ ) over  
165 MH in intralesional AUC augmentation (**Figure 5A**). To then examine whether intralesional or  
166 perilesional AUC augmentation might be favored for one or both of the contrast agents, we  
167 calculated the ratio of intralesional FUS-mediated AUC enhancement over perilesional FUS-  
168 mediated AUC enhancement. Resultant values  $>1$  suggest greater relative intralesional  
169 amplification (**Figure 5C**). By this metric, GDS exhibited greater relative FUS-mediated  
170 augmentation of delivery to the intralesional space when compared to MH (**Figure 5C**). We then  
171 repeated this analysis using maximum concentration as the key metric. As with the AUC  
172 comparisons, there was no difference between the 2 contrast agents with respect to FUS-  
173 mediated intralesional (**Figure 5D**) and perilesional (**Figure 5E**) delivery augmentation, but there  
174 was greater relative amplification of delivery to the intralesional space for GDS (**Figure 5F**).  
175 Finally, we compared post-FUS times to maximum concentration in the intralesional and  
176 perilesional spaces for MH and GDS (**Figure 5G and 5H**). For both regions, GDS reached its  
177 maximum concentration in about 10 min after FUS, while MH concentration was typically still  
178 increasing at the final (20 min) timepoint.

179

## 180 **Discussion**

181 We previously elucidated that FUS can arrest CCM growth and formation, even in the  
182 absence of therapeutic delivery<sup>30</sup>. Here, we aimed to advance the synergistic potential for  
183 concurrent therapeutic delivery with this approach. Utilizing longitudinal T1 mapping MRI, we

184 quantified the impact of FUS on therapeutic delivery of model small molecule drugs and biologics  
185 to CCMs. Our findings revealed a significant enhancement in the delivery rate of a 1 kDa small  
186 molecule, exhibiting a 4.6-fold increase in the lesion core and a 6.7-fold increase in the  
187 perilesional space. Moreover, FUS augmented overall delivery of both the 1 kDa small molecule  
188 and a 17 kDa model biologic to CCMs, with a 2.5-fold increase for the model small molecule drug  
189 and an impressive 22-fold increase for the model biologic in the lesion core. In the perilesional  
190 space, there was a 3.1-fold increase for the model small molecule drug and a 3.8-fold increase  
191 for the model biologic. GDS reached its post-FUS maximum concentration sooner than MH,  
192 suggesting there may be a more transient delivery window for biologics. Finally, our analysis  
193 uncovered a nuanced aspect of FUS enhancement, wherein the relative FUS-mediated effect is  
194 more pronounced for the small molecule in the perilesional space and for the model biologic in  
195 the lesion core. These results collectively establish a robust foundation for employing FUS in  
196 targeted therapeutic delivery regimens to effectively mitigate CCMs.

197

## 198 **T1 Mapping MRI Enables Spatiotemporal, Intra-CCM, Delivery Comparisons**

199         Given the notable heterogeneity in baseline CCM permeability<sup>23,31,32</sup>, methods allowing for  
200 comparative measurements in the same CCMs over time are important for generating statistical  
201 power and robust conclusions. We have previously shown that T1 mapping MRI enables  
202 longitudinal and quantitative assessments of contrast agent deposition in individual CCMs<sup>31</sup>.  
203 Thus, it was reasonable to leverage this MRI approach to measure model drug delivery to CCMs  
204 with FUS. Yet another advantage of T1 mapping MRI is that it has sufficient spatial resolution to  
205 discern differences in discrete CCM tissue compartments. Indeed, the lesion core harbors  
206 mutated, cavernous vessels filled with clotted blood components, while the perilesional space  
207 surrounds the core with dense populations of astrocytes, microglia, and macrophages<sup>30,31,33</sup>.  
208 These regional differences in the CCM microenvironment pose varying biotransport challenges  
209 that can influence the efficacy of different delivery approaches and molecule sizes. T1 mapping

210 MRI enabled us to measure the exact concentration of MH and GDS in both the intralesional and  
211 perilesional spaces of the CCM microenvironment, both with and without FUS.

212

### 213 **Differential Spatial Delivery Augmentation for Varying-Sized Molecules with FUS**

214 One unexpected and potentially important finding that arose from our spatiotemporally  
215 detailed T1 mapping results was that FUS differentially augments the delivery of small and large  
216 molecules to the two pre-defined CCM tissue compartments (i.e. lesion core vs. perilesional  
217 space). Specifically, FUS provided a greater relative benefit for (i) model small molecule drug  
218 delivery to the perilesional space and (ii) model biologic delivery to the lesion core. This effect is  
219 evident when using either AUC (**Figure 5C**) or maximum concentration (**Figure 5F**) as the metric  
220 of interest. To explore the potential causes behind the observed differential spatial delivery of  
221 varying-sized molecules with FUS, we first emphasize that FUS is known to offer varying degrees  
222 of benefit based on the transport properties of a given molecule<sup>34</sup>. Noting that the increase in  
223 permeability induced by FUS had a greater effect for MH in the perilesional space, we postulate  
224 that the benefit of FUS for small molecule drug delivery in regions with an already disrupted BBB  
225 (e.g. the lesion core) is less than in areas that have a more intact BBB (e.g. the perilesional  
226 space). Conversely, for a larger molecule like GDS (17 kDa; 5 nm), crossing the disrupted BBB  
227 in the lesion core may be less feasible due to biophysical constraints limiting the transport of a  
228 larger molecule. FUS partially alleviates these constraints, ultimately providing more relative  
229 benefit for larger molecules than for small molecules in the already leaky CCM core. In perilesional  
230 regions harboring a more intact BBB, even small molecules cannot effectively cross into the brain  
231 parenchyma. Thus, FUS yields a larger benefit for small molecule delivery in this region.  
232 Moreover, for larger molecules, the advantage of FUS may be less pronounced in regions with a  
233 previously intact BBB than in regions with a previously disrupted BBB, once again due to  
234 increased biophysical transport constraints.

235 We also note that differences in BBB closure time, as well as clearance mechanisms within  
236 the CCM microenvironment, for small molecules and biologics could impact the integrated  
237 exposure of tissue to drug. Here, GDS reached its maximum concentration at ~10 minutes after  
238 FUS (**Figure 5G and 5H**), while MH concentration was often still increasing at 20 min after FUS.  
239 This is consistent with the hypothesis that the BBB in and around CCMs closes fairly rapidly to  
240 larger therapeutics, which could factor into how injections are timed with respect to FUS  
241 application. Regarding clearance, while there is evidence that FUS alters clearance mechanisms  
242 through modification of the glymphatic system<sup>35-37</sup> and BBB efflux pumps<sup>38,39</sup>, its specific influence  
243 on the clearance of varying-sized molecules remains unclear. Our data indicate that GDS  
244 concentrations rapidly decrease without FUS when compared to MH without FUS or GDS with  
245 FUS, highlighting that differential clearance is also likely a significant determinant of tissue-drug  
246 exposure.

247

#### 248 **Potential for Clinical Impact on Therapeutic Delivery in CCM**

249 Here, we demonstrate that FUS enhances therapeutic delivery for molecules of different  
250 sizes in both the CCM core and surrounding perilesional space. In the clinic, this will translate to  
251 increased local delivery for any given standard systemic dose, thereby increasing therapeutic  
252 index. Furthermore, enhanced on-target drug delivery reduces the risk of side effects associated  
253 with off-target delivery. The greater benefit observed for larger molecules with FUS opens the  
254 door for biologic delivery exploration for CCM. Indeed, our study highlights that, in the absence of  
255 FUS, the delivery of a 5 nm model biologic drug (GDS) is minimal. There also may be rapid  
256 clearance from both the intralesional and perilesional spaces. However, with FUS, biologic-sized  
257 molecules are more effectively retained in both CCM compartments. These findings pave the way  
258 for future investigation into even larger agents with promising therapeutic potential for CCM, such  
259 as antibodies and gene therapy vectors.

260 Notably, FUS also offers a level of precision that can be customized for either familial or  
261 sporadic cases of CCM. In these studies, we induce BBB opening in a substantial volume—almost  
262 one-quarter—of the CCM brain. In contrast, our previous study showcased targeting FUS to a  
263 smaller volume of the CCM brain<sup>30</sup>. For patients, FUS can be tailored to target a large volume,  
264 which may be necessary for familial patients with multiple CCMs, or it can be focused on a singular  
265 CCM, as would be needed for sporadic cases. Moreover, the region of delivery can also be  
266 adapted for the mechanism of action of the delivered therapeutic. Drugs with a preventative effect  
267 could be more widely delivered than those with specific corrective functions in the CCM  
268 microenvironment. Ultimately, given its ability to stabilize lesions and seamlessly integrate with  
269 therapeutic delivery, FUS may offer a powerful platform for the treatment of CCM via image-  
270 guided drug and gene delivery.

271

## 272 **Materials and Methods**

### 273 **Animals**

274 All animal experiments adhered to ethical guidelines and were approved by the University  
275 of Virginia Animal Care and Use Committee. The animals were housed in accordance with  
276 standard laboratory conditions, maintaining a temperature of 22°C and a 12-hour light/12-hour  
277 dark cycle. The generation of the CCM murine model was established as previously detailed<sup>31</sup>.  
278 Briefly, *Krit1*<sup>fl/null</sup> or *Krit1*<sup>fl/fl</sup> male or females were generated under the endothelial promoter  
279 *Pdgfb*<sup>CreER</sup>. On postnatal day 5, induction of *Krit1* was initiated with a subcutaneous injection of  
280 tamoxifen (50 µL at 2mg/mL in corn oil). Genotypes were subsequently verified using Transnetyx  
281 (Cordova, TN). Mice were studied between 2 and 3 months old.

282

### 283 **MRI Acquisition**

284 Data for T1 maps were acquired with a set of multi-slice 2D spin echo (SE) images at  
285 varied repetition times (TR) to generate a saturation recovery curve. 2 sets of 7 images, for a total

286 of 14 scans, were acquired prior to FUS and contrast agent administration to obtain saturation  
287 recovery curves with a satisfactory dynamic range. The two sets of image series were offset by  
288 the slice thickness in the slice select plane to ensure 3D coverage of the brain. The parameters  
289 for these scans were: TR=790, 1040, 1350, 1750, 2300, 3215, and 7000 ms, TE=6.71 ms, slice  
290 thickness=0.6 mm, slice gap=0.6 mm, FOV=35 x 35 mm, matrix size=180 x 180, rare factor=10,  
291 and R= 0.194 x 0.194 x 0.6 mm<sup>3</sup>. After FUS and contrast agent administration, 14 SE images  
292 were acquired with identical parameters except at a fixed TR=1040 ms. The acquisitions  
293 alternated between slice package orientations resulting in 7 images at each slice profile geometry.  
294 Time per acquisition was 1 minute and 28 seconds.

295

## 296 Data Processing

297 A saturation recovery approach was utilized to calculate  $M_0$  and all T1 values (pre and  
298 post contrast) on a voxel-by-voxel basis by fitting the data to the signal equation:

299

$$300 \quad |S| = M_0 \left( 1 - e^{-\frac{TR}{T_1}} \right) e^{-\frac{TE}{T_2}} \quad \text{Eqn [1]}$$

301

302 In equation 1,  $|S|$  is the magnitude of the signal within the voxel,  $M_0$  is the product of the thermal  
303 equilibrium magnetization and coil sensitivity, TR is the repetition time (ms), T1 is the spin-lattice  
304 relaxation (ms), TE is the echo time (ms), and T2 is the spin-spin relaxation (ms). The echo time  
305 exponential is assumed to be 1 due to  $TE \ll T_2$ , resulting in the final form seen in equation 2.

306

$$307 \quad |S| = M_0 \left( 1 - e^{-\frac{TR}{T_1}} \right) \quad \text{Eqn [2]}$$

308

309 A custom MATLAB script fit the signal magnitude data on a voxel-by-voxel basis to equation 2.

310 Each fitting procedure simultaneously fit the data to 8 functions: function 1 incorporated the 7 pre-



311 contrast variable TR scans, while functions 2-8 incorporated the singular scan at a fixed TR but  
312 different time points. The fits were constrained to having the same  $M_0$  value but allowed different  
313 T1 values. Pre-contrast and post-contrast T1 values were then used to calculate the contrast  
314 agent concentration on a voxel-by-voxel basis at each time point using equation 3.

315

316 
$$\frac{1}{T_{1\_Post}} = \frac{1}{T_{1\_Pre}} + r_1 C_1 \text{ Eqn [3]}$$

317

318 In equation 3,  $T_{1\_Post}$  is the post-contrast value at a particular time point (ms),  $T_{1\_Pre}$  is the pre-  
319 contrast T1 value (ms),  $r_1$  is the contrast agent relaxivity (L/mmol/ms), and  $C_1$  is the contrast  
320 agent concentration (mM). At the conclusion of this process, concentration values for slice  
321 package 1 existed for time points (minutes): 1.47, 4.40, 7.33, 10.27, 13.2, 16.13, and 19.07, while  
322 concentration values for slice package 2 existed for time points (minutes): 2.93, 5.87, 8.80, 11.73,  
323 14.67, 17.60, and 20.53. To obtain 3D coverage at each time point, concentration data was  
324 calculated at the missing time points by linearly interpolating between the acquired points. This  
325 required an assumption of 0 concentration at minute 0 for slice package 2. The 20.53-minute time  
326 point was not used because it required data be extrapolated past minute 19.07 for slice package  
327 1.

328 A second custom MATLAB script was used to calculate average concentrations with  
329 manually drawn regions of interest (ROIs) on the concentration maps. To ensure the iron rich  
330 intralesional data was not skewed by susceptibility artifacts, a data exclusion method was  
331 developed. Briefly, a ROI of healthy brain tissue on the contralateral hemisphere was used to  
332 calculate an average residuals value for the fit. If any residuals value for the voxels within the  
333 lesion core were 3 times greater than this average, they were excluded from the analysis. The  
334 value of 3 was empirically determined. To maintain consistency within data processing, this was  
335 also applied to all perilesional data.

336

### 337 **FUS Blood-Brain Barrier Opening**

338         The FUS procedure was conducted using the RK-300 small bore FUS device (FUS  
339 Instruments, Toronto, CA). Mice were prepared by shaving and depilating their heads before  
340 being placed in a supine position and coupled to the transducer using degassed ultrasound gel.  
341 Blood-brain barrier opening was achieved using a 1.1 MHz single-element transducer with a 10  
342 ms burst length over a 2000 ms period. A total of 60 sonications were administered during a 2-  
343 minute sonication duration. The FUS Instruments software, operating in the "Blood-brain Barrier"  
344 mode, facilitated PCD-modulated PNP. The feedback control system parameters were set as  
345 follows: a starting pressure of 0.2 MPa, pressure increment of 0.05 MPa, maximum pressure of  
346 0.4 MPa, 20 sonication baselines without microbubbles, area under the curve (AUC) bandwidth  
347 of 500 Hz, AUC threshold of 10 standard deviations, pressure drop of 0.95, and frequency  
348 selection of the subharmonic, first ultraharmonic, and second ultraharmonic. Optison™ (GE  
349 HealthCare) microbubbles were intravenously injected as a bolus dose of  $10^5$  microbubbles per  
350 gram of body weight. Prior to sonication, the distribution of microbubble diameter and  
351 concentration was assessed using a Coulter counter (Multisizer 3; Beckman Coulter, Fullerton,  
352 California). T1 mapping MRI sequences were used to guided sonication targeting. Six non-  
353 overlapping sonication targets were placed over one frontal hemisphere with placement optimized  
354 to target CCMs.

355

### 356 **Contrast Agent Injections**

357         MultiHance® (gadobenate dimeglumine; Bracco) and GadoSpin D™ (dendritic Gd-  
358 chelate; Viscover) were injected as a bolus intravenously at a dose of 0.01 and 0.0002 mmol,  
359 respectively, diluted in saline. Injection of contrast agent was given immediately prior to MRI  
360 acquisition for FUS- control studies and immediately following the initiation of FUS for FUS+  
361 studies.

362

### 363 **Passive Cavitation Detection**

364 Acoustic emissions during FUS were detected with a fiber-optic hydrophone (Precision  
365 Acoustics, Dorset, UK) of 10  $\mu\text{m}$  diameter and 15 mm aperture center-mounted within the  
366 ultrasound transducer. Emissions data was processed with a custom MATLAB script. The area  
367 under the curve of the acoustic emissions at the subharmonic (0.5f) and ultra-harmonics (1.5f,  
368 2.5f) after applying a 300 Hz bandwidth filter. Broadband emissions were evaluated by summing  
369 acoustic emissions following the removal of all emissions at the fundamental frequency,  
370 harmonics (2f, 3f, 4f), subharmonic (0.5f), and ultra-harmonics (1.5f, 2.5f, 3.5f).

371

### 372 **Statistical Analysis**

373 All results reported with error bars are means with standard deviation. The “n” values per  
374 group are made evident either by individual data points shown or statement of “n” value in figure  
375 or figure legend. Statistical significance was assessed at  $p < 0.05$  for all experiments and were  
376 calculated using GraphPad Prism 9 (San Diego, USA). Statistical tests are provided in the figure  
377 legends.

378

### 379 **Author Contributions**

380 DGF, MH, and RJP conceptualized the study. DGF and MH conducted the FUS experiments with  
381 the aid of CMG in animal preparation. MRI sequences and analysis were optimized by MH and  
382 GWM. MRI data was acquired and processed by MH and analyzed by DGF and MH. KAS  
383 generated experimental animals. DGF and MH designed the figures and wrote the manuscript.  
384 GWM, PT, and RJP edited the manuscript. All authors approved the manuscript.

385

386

387

388 **Acknowledgements**

389 This work was supported by funding from NIH R01CA279134, R01EB030409, R01EB030744,  
390 and R21NS118278 to RJP; NIH R21NS116431 and grants from Focused Ultrasound Foundation,  
391 Be Brave for Life Foundation, and Alliance to Cure Cavernous Malformation to PT; NIH  
392 R01CA226899 to GWM; and American Heart Association 830909 to DGF. We thank Dr. Kevin  
393 Whitehead for kindly providing the mouse strains used in this study. We are also grateful to the  
394 University of Virginia Molecular Imaging Core and Jeremy Gatesman of the University of Virginia  
395 Center for Comparative Medicine for assistance with MRI imaging and catheterization  
396 procedures, respectively.

397

398 **References**

- 399 1. Snellings, D. A. *et al.* Cerebral Cavernous Malformation: From Mechanism to Therapy.  
400 *Circ. Res.* **129**, 195–215 (2021).
- 401 2. Denier, C. *et al.* Clinical features of cerebral cavernous malformations patients with  
402 KRIT1 mutations. *Ann. Neurol.* **55**, 213–220 (2004).
- 403 3. Gault, J., Sain, S., Hu, L. J. & Awad, I. A. Spectrum of genotype and clinical  
404 manifestations in cerebral cavernous malformations. *Neurosurgery* **59**, 1278–1284  
405 (2006).
- 406 4. Gianfrancesco, F. *et al.* Highly variable penetrance in subjects affected with cavernous  
407 cerebral angiomas (CCM) carrying novel CCM1 and CCM2 mutations. *Am. J. Med.*  
408 *Genet. B. Neuropsychiatr. Genet.* **144B**, 691–695 (2007).
- 409 5. Awad, I. A. & Polster, S. P. Cavernous angiomas: deconstructing a neurosurgical  
410 disease: JNSPG 75th Anniversary Invited Review Article. *J. Neurosurg.* **131**, 1–13  
411 (2019).
- 412 6. Amin-Hanjani, S., Ogilvy, C. S., Ojemann, R. G. & Crowell, R. M. Risks of surgical  
413 management for cavernous malformations of the nervous system. *Neurosurgery* **42**,  
414 1220–1228 (1998).
- 415 7. Hong, T. *et al.* Somatic MAP3K3 and PIK3CA mutations in sporadic cerebral and spinal  
416 cord cavernous malformations. *Brain* **144**, 2648–2658 (2021).
- 417 8. Zhou, Z. *et al.* Cerebral cavernous malformations arise from endothelial gain of MEKK3-  
418 KLF2/4 signalling. *Nature* **532**, 122–126 (2016).
- 419 9. Tang, A. T. *et al.* Endothelial TLR4 and the microbiome drive cerebral cavernous  
420 malformations. *Nature* **545**, 305–310 (2017).
- 421 10. Li, W. *et al.* Propranolol inhibits cavernous vascular malformations by  $\beta$ 1 adrenergic  
422 receptor antagonism in animal models. *J. Clin. Invest.* **131**, (2021).
- 423 11. Shi, C. *et al.* B-Cell Depletion Reduces the Maturation of Cerebral Cavernous

- 424 Malformations in Murine Models. *J. Neuroimmune Pharmacol.* **11**, 369–377 (2016).
- 425 12. Gibson, C. C. *et al.* Strategy for identifying repurposed drugs for the treatment of cerebral  
426 cavernous malformation. *Circulation* **131**, 289–299 (2015).
- 427 13. Shenkar, R. *et al.* Rho kinase inhibition blunts lesion development and hemorrhage in  
428 murine models of aggressive Pcd10/Ccm3 disease. *Stroke* **50**, 738–744 (2019).
- 429 14. McKerracher, L. *et al.* A Brain-Targeted Orally Available ROCK2 Inhibitor Benefits Mild  
430 and Aggressive Cavernous Angioma Disease. *Transl. Stroke Res.* **11**, 365–376 (2020).
- 431 15. Shenkar, R. *et al.* RhoA Kinase Inhibition With Fasudil Versus Simvastatin in Murine  
432 Models of Cerebral Cavernous Malformations. *Stroke* **48**, 187–194 (2017).
- 433 16. Lopez-Ramirez, M. A. *et al.* Cerebral cavernous malformations form an anticoagulant  
434 vascular domain in humans and mice. *Blood* **133**, 193–204 (2019).
- 435 17. Polster, S. P. *et al.* Atorvastatin Treatment of Cavernous Angiomas with Symptomatic  
436 Hemorrhage Exploratory Proof of Concept (AT CASH EPOC) Trial. *Neurosurgery* **85**, 843  
437 (2019).
- 438 18. Hong, C. C. *et al.* Cerebral cavernous malformations are driven by ADAMTS5 proteolysis  
439 of versican. *J. Exp. Med.* **217**, (2020).
- 440 19. Detter, M. R. *et al.* Novel Murine Models of Cerebral Cavernous Malformations.  
441 *Angiogenesis* **23**, 651–666 (2020).
- 442 20. Cardoso, C. *et al.* Novel Chronic Mouse Model of Cerebral Cavernous Malformations.  
443 *Stroke* **51**, 1272–1278 (2020).
- 444 21. Mikati, A. G. *et al.* Dynamic Permeability and Quantitative Susceptibility. *Stroke* **45**, 598–  
445 601 (2014).
- 446 22. Girard, R. *et al.* Vascular permeability and iron deposition biomarkers in longitudinal  
447 follow-up of cerebral cavernous malformations. *J. Neurosurg.* **127**, 102–110 (2016).
- 448 23. Mikati, A. G. *et al.* Vascular permeability in cerebral cavernous malformations. *J. Cereb.*  
449 *Blood Flow Metab.* **35**, 1632–1639 (2015).

- 450 24. Yadla, S. *et al.* Cerebral cavernous malformations as a disease of vascular permeability:  
451 from bench to bedside with caution. *Neurosurg. Focus* **29**, 1–7 (2010).
- 452 25. Gorick, C. M. *et al.* Applications of focused ultrasound-mediated blood-brain barrier  
453 opening. *Adv. Drug Deliv. Rev.* **191**, 114583 (2022).
- 454 26. Fisher, D. G. & Price, R. J. Recent Advances in the Use of Focused Ultrasound for  
455 Magnetic Resonance Image-Guided Therapeutic Nanoparticle Delivery to the Central  
456 Nervous System. *Front. Pharmacol.* **10**, (2019).
- 457 27. Timbie, K. F., Mead, B. P. & Price, R. J. Drug and gene delivery across the blood-brain  
458 barrier with focused ultrasound. *J. Control. Release* **219**, 61–75 (2015).
- 459 28. Shang, X., Wang, P., Liu, Y., Zhang, Z. & Xue, Y. Mechanism of low-frequency  
460 ultrasound in opening blood-tumor barrier by tight junction. *J. Mol. Neurosci.* **43**, 364–369  
461 (2011).
- 462 29. Sheikov, N. *et al.* Brain arterioles show more active vesicular transport of blood-borne  
463 tracer molecules than capillaries and venules after focused ultrasound-evoked opening of  
464 the blood-brain barrier. *Ultrasound Med. Biol.* **32**, 1399–1409 (2006).
- 465 30. Fisher, D. G. *et al.* Focused Ultrasound Blood-Brain Barrier Opening Arrests the Growth  
466 and Formation of Cerebral Cavernous Malformations. *bioRxiv* 2024.01.31.577810 (2024).
- 467 31. Fisher, D. G. *et al.* Magnetic Resonance Imaging of Mouse Cerebral Cavernomas Reveal  
468 Differential Lesion Progression and Variable Permeability to Gadolinium. *Arterioscler.*  
469 *Thromb. Vasc. Biol.* **43**, 958–970 (2023).
- 470 32. Hart, B. L., Taheri, S., Rosenberg, G. A. & Morrison, L. A. Dynamic Contrast-Enhanced  
471 MRI Evaluation of Cerebral Cavernous Malformations. *Transl. Stroke Res.* **4**, 500–506  
472 (2013).
- 473 33. Plummer, N. W. *et al.* Loss of p53 Sensitizes Mice with a Mutation in Ccm1 (KRIT1) to  
474 Development of Cerebral Vascular Malformations. *Am. J. Pathol.* **165**, 1509–1518 (2004).
- 475 34. Marty, B. *et al.* Dynamic study of blood-brain barrier closure after its disruption using

- 476 ultrasound: A quantitative analysis. *J. Cereb. Blood Flow Metab.* **32**, 1948–1958 (2012).
- 477 35. Lee, Y. *et al.* Improvement of glymphatic–lymphatic drainage of beta-amyloid by focused  
478 ultrasound in Alzheimer’s disease model. *Sci. Rep.* **10**, (2020).
- 479 36. Meng, Y. *et al.* Glymphatics Visualization after Focused Ultrasound-Induced Blood–Brain  
480 Barrier Opening in Humans. *Ann. Neurol.* **86**, 975–980 (2019).
- 481 37. Han, M., Seo, H., Choi, H., Lee, E. H. & Park, J. Localized Modification of Water Molecule  
482 Transport After Focused Ultrasound-Induced Blood–Brain Barrier Disruption in Rat Brain.  
483 *Front. Neurosci.* **15**, (2021).
- 484 38. Aryal, M. *et al.* Effects on P-Glycoprotein Expression after Blood-Brain Barrier Disruption  
485 Using Focused Ultrasound and Microbubbles. *PLoS One* **12**, e0166061 (2017).
- 486 39. Cho, H. S. *et al.* Localized Down-regulation of P-glycoprotein by Focused Ultrasound and  
487 Microbubbles induced Blood-Brain Barrier Disruption in Rat Brain. *Sci. Rep.* **6**, 1–10  
488 (2016).
- 489
- 490



